Supplementary Information

Robust Wrinkled MoS_2/N-C Bifunctional Electrocatalysts Interfaced with Single Fe Atoms for Wearable Zinc-Air Batteries

Yan Yan,[1, 2] Shuang Liang,[1] Xiang Wang,[3] Mingyue Zhang,[1] Shu-Meng Hao,[1] Xun Cui,[1] Zhiwei Li,[4] and Zhiqun Lin[1]*

1. School of Materials Science and Engineering, Georgia Institute of Technology, Atlanta, GA 30332, USA

2. School of Chemistry & Materials Science, Jiangsu Key Laboratory of Green Synthetic Chemistry for Functional Materials, Jiangsu Normal University, Xuzhou 221116, China.

3. Chemical Sciences Division, Oak Ridge National Laboratory, Oak Ridge, TN, 37831, USA.

4. Shenzhen Cloud Computing Center, National Supercomputing Center, Shenzhen 518055, China.

⋆Corresponding Authors: zhiqun.lin@mse.gatech.edu

Experimental Section

1. Materials

Ammonium molybdate ($(NH_4)_6Mo_7O_{24}\cdot 4H_2O$, 99%), dicyandiamide ($C_2H_4N_4$, 99%) and iron (III) chloride hexahydrate ($FeCl_3\cdot 6H_2O$, 99%) were purchased from Alfa Aesar. Thiourea (NH_2CSNH_2, 99%), Polyvinyl Pyrrolidone (PVP, Mw~55000 Da), dopamine hydrochloride ($C_8H_{12}ClNO_2$, 99%) was purchased from Sigma-Aldrich. Commercial Pt/C (20wt%) catalyst was purchased from Sigma-Aldrich. Commercial Ir/C (20wt%) catalyst was purchased from Premetek Co. All chemicals were used as received without further purification

2. Preparation of MoS_2 nanospheres (denoted MoS_2 NSs)

In a typical reaction, 617 mg (0.5 mmol) ammonium molybdate ($(NH_4)_6Mo_7O_{24}\cdot 4H_2O$), 533 mg (7 mmol) thiourea (NH_2CSNH_2,), and 300 mg (0.005 mmol) surfactant PVP were dissolved in 17 mL of deionized water under vigorous stirring to form a homogeneous solution. Then, the solution was transferred into a 50 mL Teflon-lined stainless steel autoclave and kept at 220 °C for 18 h. After being cooled to room temperature, the generated precipitates were centrifuged and washed with water and ethanol several times. The final products were dried at 50 °C under vacuum for 12 h.

3. Preparation of polydopamine coated MoS_2 NSs (MoS_2@PDA NSs)

The MoS_2 NS coated with PDA (denoted MoS_2@PDA) were synthesized by polymerization of dopamine in Tris buffer (pH 8.5). In a typical procedure, 100 mg MoS_2 NS was dispersed in 20 mL Tris buffer (pH 8.5), and 20 mg dopamine hydrochloride was added in the solution to form a mixture. The mixture was stirred at room temperature for 15 h, and the suspension was centrifuged and washed with water several times. The final products were dried at room temperature under vacuum for 12 h.

4. Preparation of MoS_2@Fe-N-C NSs, MoS_2@Co-N-C NSs and MoS_2@Ni-N-C NSs

The MoS_2 NS covered with atomic Fe, N-co-dopped carbon shell was crafted according to the following steps. 250 mg dicyandiamide (DICY) was dispersed into 10 mL deionized water containing 50 mg $FeCl_3$, forming a uniform solution. 100 mg of MoS_2@PDA was then introduced into the above solution and stirred for 3 h. Afterwards, the obtained suspension was vacuum-dried at 50 °C, followed by heat treatment at 800 °C for 2 h under N_2 atmosphere.

Likewise, MoS_2@Co-N-C NSs and MoS_2@Ni-N-C NSs were also crafted using the same procedure, in which $FeCl_3$ was replaced with $CoCl_2$ and $NiCl_2$, respectively.

5. Characterization

Scanning electron microscopy (SEM) measurements were performed using a field emission source operated at an accelerating voltage of 15 kV by JEOL JSM-6700F. The elemental mapping was recorded using energy dispersive X-ray spectrometry (EDS) with the abovementioned SEM.

The transmission electron microcopy (TEM, JEM-100CX11 microscope, 100 kV) and high-resolution TEM (HRTEM, Hitachi HD-2700) samples were prepared by dispersing products of interest in ethanol via ultrasonication, followed by the deposition on a carbon film-supported copper grid. Powder X-ray diffraction (XRD, Rigaku D/max-2400) measurements were conducted using Cu-Kα radiation (40 kV, 120 mA) with a step of 0.08° per 25 s and a 2θ range of 10-80°. Raman spectroscopy study was performed on a Renishaw InVia Raman spectrometer equipped with a 532 nm laser. Fourier transform infrared (FTIR) spectra were collected by JASCO FTIR 6300. X-ray photoelectron spectroscopy (XPS) measurements were carried out on a Thermo K-alpha electron spectrometer with Al Kα radiation. XAFS measurements were performed at the beamline 10ID-B of the Advanced Photon Source at Argonne National Laboratory. Spectra were collected at Fe K-edge (eV) in transmission mode with each Fe_2O_3 and Fe foil collected simultaneously and used as the reference for energy calibration as well as data analysis.

6. Electrochemical Measurements

The catalyst ink recipe was mildly sonicated overnight and optimized for homogeneity before being coated on a mirror-polished glassy carbon working electrode (0.196 cm^2). To avoid mass transport limitation, which is often caused by nonuniform catalyst film, a homogeneous film was ensured by drying the catalyst ink (10 μL) on the electrode at room temperature. Commercially acquired Ir/C and Pt/C (20 wt%) were used as reference catalysts. A graphite rod (99.999%) was used as the counter electrode and Ag/AgCl as reference electrode. The measured potentials are referred to the RHE, $E_{RHE} = E_{Ag/AgCl} + 0.059pH + E^{\theta}_{Ag/AgCl}$. Koutechy-Levich plots (J^{-1} vs. ω^{-1}) in the inset of **Figure 4d** were analyzed at various electrode potentials. The slopes of their best linear fit lines were used to calculate the number of electrons transferred (n) based on the equation below.

$$\frac{1}{J} = \frac{1}{J_L} + \frac{1}{J_K} = \frac{1}{B\omega^{\frac{1}{2}}} + \frac{1}{J_K} \tag{S1}$$

$$B = 0.62\mathrm{n}FC_0(D_0)^{\frac{2}{3}}\nu^{-\frac{1}{6}} \tag{S2}$$

$$J_K = \mathrm{n}FkC_0 \tag{S3}$$

where J is the measured current density; J_K and J_L are the kinetic- and diffusion-limiting current densities, respectively; ω is the angular velocity; n is the transferred electron number; F is the Faraday constant; C_o is the bulk concentration of O_2; v is the kinematic viscosity of the electrolyte; and k is the electron-transfer rate constant.

The ORR polarization curves were recorded in 0.1 M KOH at the scan rate of 5 mV s^{-1} at room temperature on a three-electrode workstation. The OER polarization curves were tested in 1 M KOH. Bifunctional ORR and OER properties were evaluated in 0.1 m KOH solution at room temperature. Any capacitive current contributions were eliminated via iR correction by deducting the background current from the measured currents.

The air-cathodes for primary Zn–air battery (ZAB) were prepared by coating the catalysts (0.25 mg cm^{-2}) on a hydrophobic carbon cloth and evaluated in 6 m KOH electrolyte containing 0.2 M ZnAc. The fabricated all-solid-state battery and liquid-state electrolyte battery were assembled and tested under ambient conditions. No inert atmosphere or glove box was used.

7. Assembly and Test of Wearable Solid-State Zn-Air Batteries (ZABs)

The wearable solid-state Zn-air battery (ZAB) was fabricated in a sandwich structure. Particularly, a polished zinc foil (0.05 mm thickness), the catalysts coated carbon cloth (0.25 mg cm^{-2}) and a polyvinyl alcohol (PVA) gel were used as anode, air electrode and solid electrolyte, respectively. The gel polymer electrolyte was prepared as follows: polyvinyl alcohol (PVA, 5 g) was dissolved in 50 mL 18 M KOH at 95 °C to form a homogeneous viscous solution, followed by casting on a glass disk to form a thin polymer film. The film was then frozen in a freezer at -20 °C about 2 h, and then kept at 0 °C for 4 h. The film was thawed for 12 h prior to use. The air electrode (cathode) was prepared as follows: the as-prepared catalysts or Pt/C+Ir/C (1:1), carbon black (CB) and polyvinylidene fluoride (PVDF) with mass ratio of 8:1:1 was well-dispersed in dimethylpyrazole (200 mg mL^{-1}) to form a homogeneous suspension. Then, the suspension was casted onto carbon cloth with a mass loading of 0.25 mg cm^{-2}. The samples were dried at room temperature before test. Then, cathode and anode were placed on the two sides of PVA gel. And a glass fiber separator was used between the gel electrolyte and flexible cathode, in order to prevent the contact between the soft cathode and anode. All tests for the wearable Zn-air battery were performed on a battery test station (Land). Cycling test was performed using recurrent galvanostatic pulses for 10 min of discharge, followed by 10 min of charge.

The power density (mW cm^{-2}) was calculated according to the equation:

$$\text{current density} \times \text{discharge voltage} \tag{S4}$$

The specific capacity (mAh g^{-1}) was calculated according to the equation:

$$\frac{\text{current density} \times \text{service hours}}{\text{weight of consumed zinc}} \tag{S5}$$

The energy density (Wh kg^{-1}) was calculated according to the equation:

$$\frac{\text{current density} \times \text{service hours} \times \text{average discharge voltage}}{\text{weight of consumed zinc}} \tag{S6}$$

8. Assembly and Test of Liquid ZABs

The as-prepared catalysts and Pt/C + Ir/C based air-cathodes were used to assemble rechargeable ZABs. Zn plate (0.2 mm thickness) was used as the anode, and 6.0 M KOH electrolyte was filled between the cathode and anode. To build the rechargeable ZABs, 6.0 M KOH with 0.2 M zinc acetate was used as the electrolyte, where the zinc acetate was added to ensure reversible Zn electrochemical reactions at the anode. The method of preparing the air electrode is the same as the air electrode of solid-states ZABs. The Zn plate layer and catalyst layer have an effective area of 1.766 cm^2 and allows O_2 from ambient air to reach the catalyst sites. All tests for the wearable Zn-air battery were performed on a battery test station (Land). Cycling test was conducted using recurrent galvanostatic pulses for 1 h of discharge, followed by 1 h of charge.

9. Computational Methods

All density functional theory (DFT) calculations were implemented in the Vienna Ab initio Simulation Package (VASP).(1) The generalized gradient approximation (GGA) with Perdew-Burke-Ernzerhof (PBE) functional and the projector augmented wave (PAW) potential were used to describe the exchange-correlation energy and the electron-ion interaction, respectively.(2, 3) To ensure the accuracy of calculated results, the energy cutoff for the plane wave basis was set to 450 eV. The energy tolerance for self-consistency was set to 10^{-5} eV. The force tolerance for atomic relaxation was set to be 0.001 eV/Å.

The MoS_2 model was constructed by 4 × 4×1 primitive MoS_2 cells with a = b = 12.66 Å and γ = 120°. For the MoS_2@Fe-N-C model, to compensate for the lattice mismatch between MoS_2 (a = 3.16 Å) and graphene (a = 2.46 Å), we used a supercell comprising 4 × 4 primitive MoS_2 cells and 5 × 5 primitive graphene cells. For this supercell, the lattice mismatch is reduced to 1.9%. The Fe-N-C model was then constructed by embedding a FeN_4 site in a periodic 5×5 graphene. 4×4×1 Monkhorst-Pack k-points mesh was chosen.

The oxygen reduction reaction (ORR) and oxygen evolution reaction (OER) pathways on the considered models were calculated in details according to electrochemical framework developed by Norskov and his co-workers.(4, 5) In an alkaline electrolyte, the ORR is considered to proceed along the $4e^-$ processes as follows:

$$O_2(g) + * + e^- + H_2O\ (l) \longrightarrow OOH^* + OH^- \tag{S7}$$

$$OOH^* + e^- \longrightarrow O^* + OH^- \tag{S8}$$

$$O^* + H_2O\ (l) + e^- \longrightarrow OH^* + OH^- \tag{S9}$$

$$OH^* + e^- \longrightarrow OH^- + * \tag{S10}$$

where * represents an active site on the catalytic surface, (*l*) and (*g*) refer to liquid and gas phases, respectively.

The OER occurred through four elementary steps takes the reverse direction of the ORR shown above (Equation S7-S10).

The chemical potential for the reaction ($H^*+ e^-$) (i.e., the free energy per H) is equal to that of 1/2 H_2 by setting the reference potential to be that of the standard hydrogen electrode at standard condition.

The reaction free energy (ΔG) is further calculated by the equation:

$$\Delta G = \Delta E + \Delta ZPE - T\Delta S - qU + k_B T \ln 10 * (pH) \tag{S11}$$

where ΔE is the reaction energy of reactant and product molecules adsorbed on catalyst surface, obtained from DFT calculation. ΔZPE and ΔS are the change in zero-point energy and entropy in the reaction. U is the applied potential relative to RHE. q is the charge transfer in each elementary step.

Figures and Tables

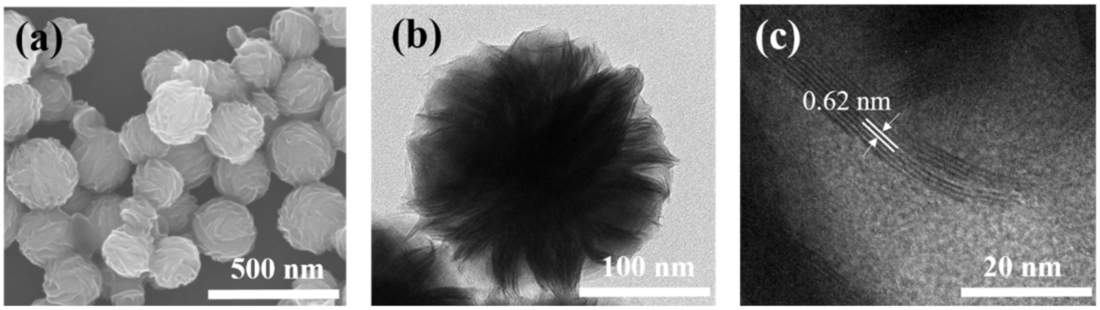

Figure S1 (a) SEM image of MoS_2 nanospheres (NSs). TEM images of MoS_2 NSs at (b) low and (c) high magnifications, respectively.

Due to high surface energy of MoS_2 nanosheets, poly(vinylpyrrolidone) (PVP) is absorbed on the surface of MoS_2 nanosheets. The absorbed PVP surfactant can efficiently protect the 2D nanosheet structure from re-stacking. Subsequently, PVP on the surface of MoS_2 drives the radially-oriented assembly of MoS_2 nanosheets into MoS_2 nanospheres (NSs). After being thoroughly washed with water, ethanol, and acetone, the radially-oriented MoS_2 NS containing a few layers of MoS_2 are obtained.

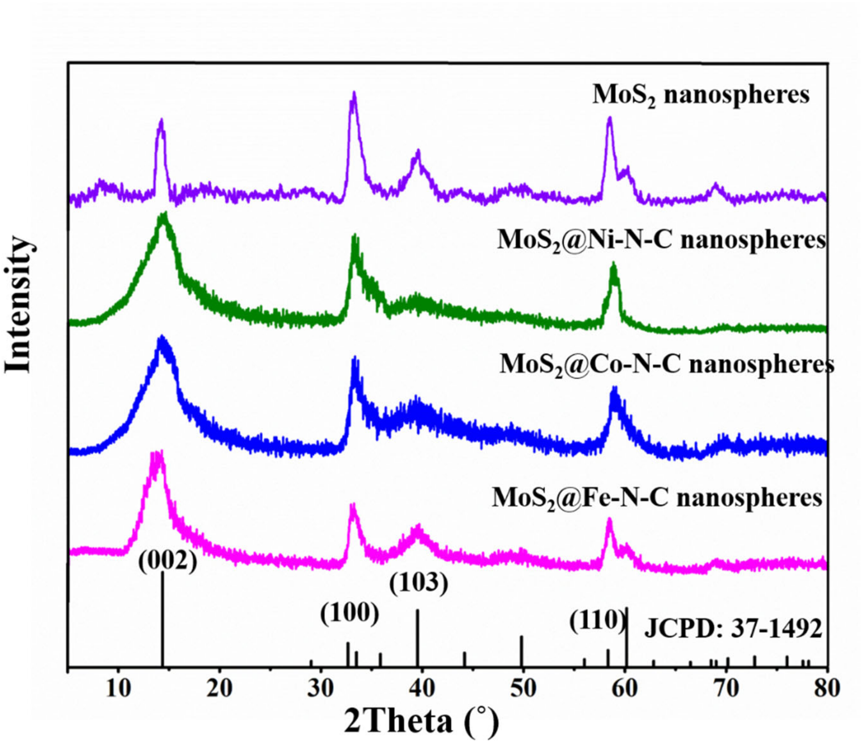

Figure S2. XRD pattern of MoS_2 NSs, MoS_2@Ni-N-C NSs, MoS_2@Co-N-C NSs, MoS_2@Fe-N-C NSs, and the standard pattern of hexagonal MoS_2 (JCPDS card No. 37-1492), respectively.

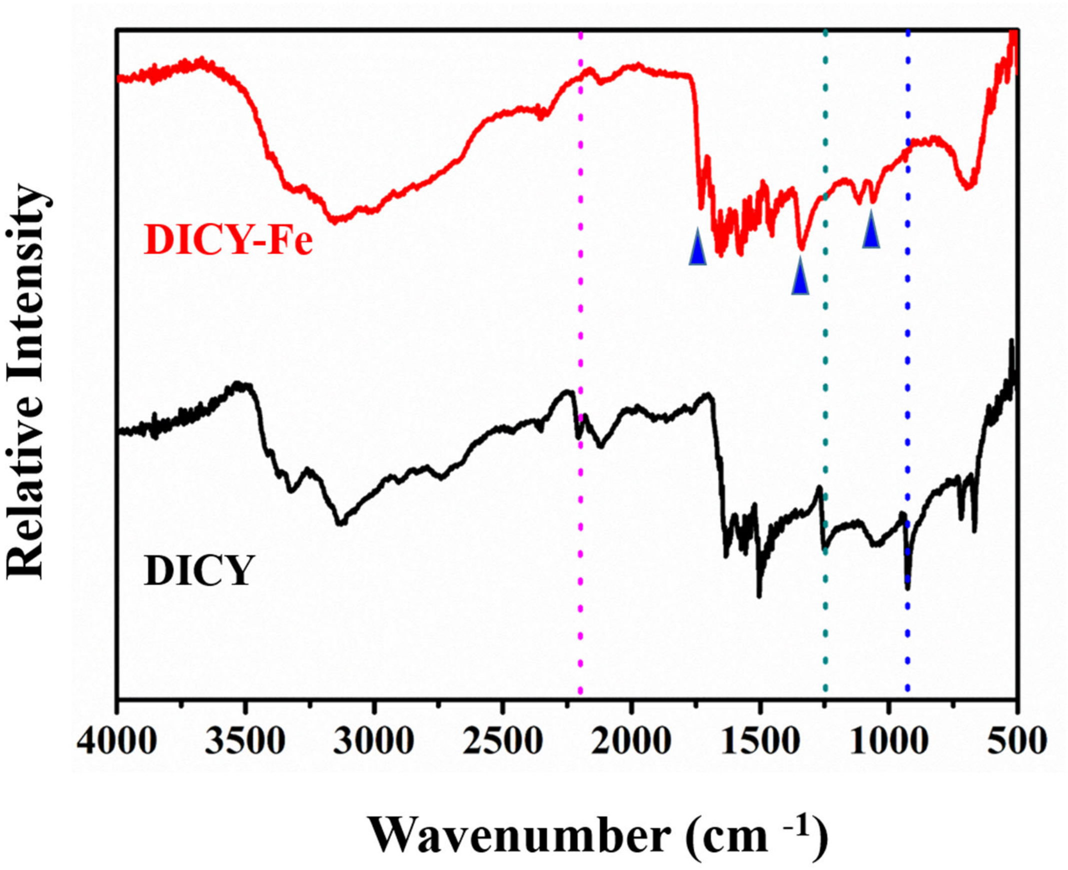

Figure S3. Fourier transform infrared (FTIR) spectra of DICY and DICY-Fe, respectively.

In the case of neat DICY (black curve), the absorption band at 2161–2209 cm^{-1} can be attributed to the C≡N stretching vibration (pink dash line). The band observed at approximately 1243 cm^{-1} is the typical C-N stretching vibration (green dash line). The absorption at 920 cm^{-1} is characteristic out-of-plane bending vibration of N-H group (blue dash line). Clearly, in DICY-Fe (red curve), new peaks near 1742, 1329 and 1110 cm^{-1} are presented, signifying the coordination interaction of Fe and DICY.

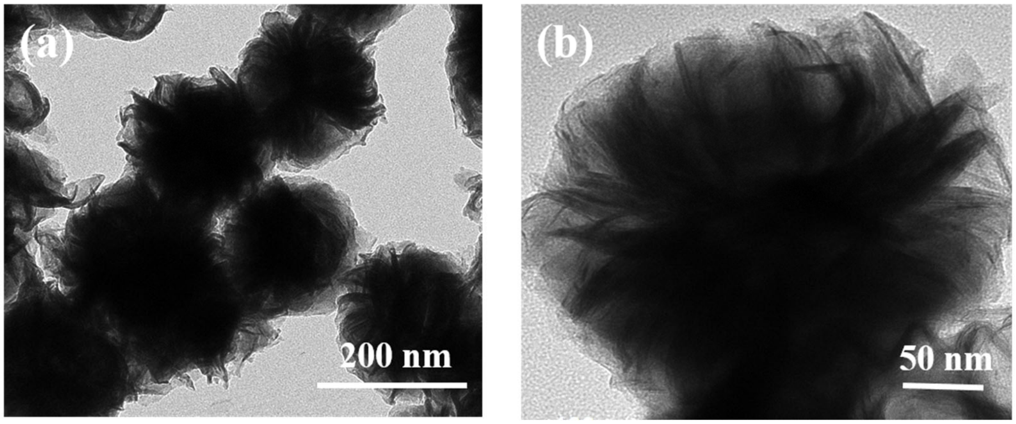

Figure S4. TEM images of MoS_2@Fe-N-C NSs at (a) low and (b) high magnifications, respectively.

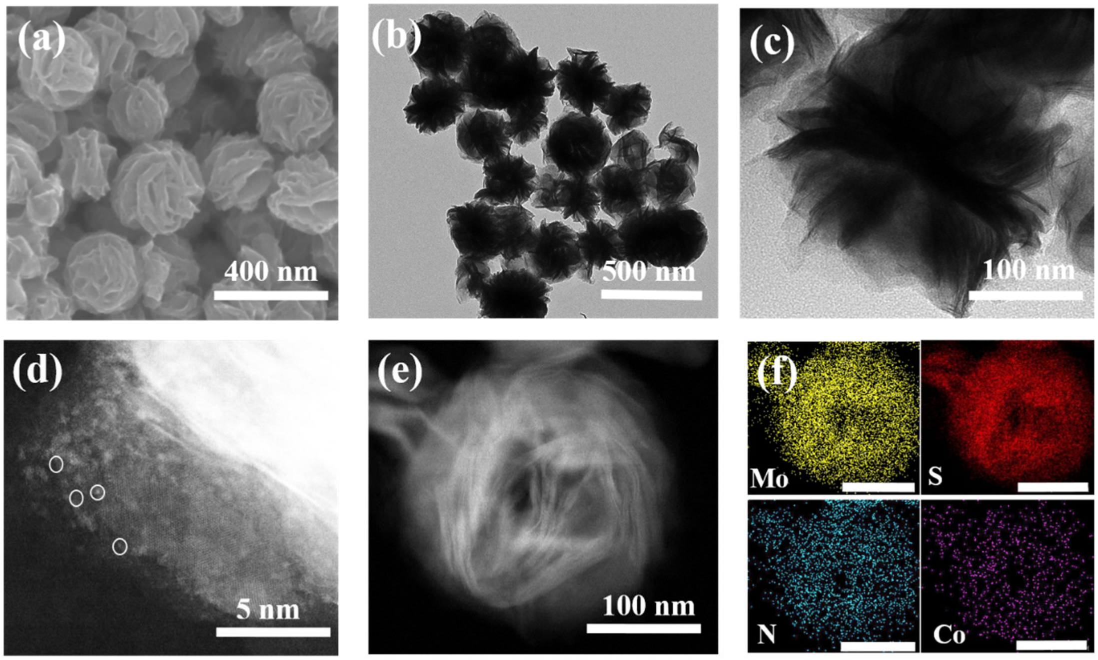

Figure S5. (a) SEM image and TEM images of MoS_2@Co-N-C NSs at (b) low and (c) high magnifications, respectively. (d) Aberration-corrected (AC) HAADF-STEM image of MoS_2@Co-N-C NS. (e) High angle annular dark field scanning TEM (HAADF-STEM) image and (f) element maps (Mo: yellow, S: red, N: blue, Co: purple; scale bar = 100 nm) of MoS_2@Co-N-C NS.

The HAADF-STEM images of MoS_2@Co-N-C NSs present atomically-dispersed species in the carbon substrate. The element mapping results reveal the homogeneous distribution of Mo, S, N and Co elements in the respective NSs (**Figure S5f**). These results suggest that single Co atoms were successfully anchored on the N-doped carbon matrix.

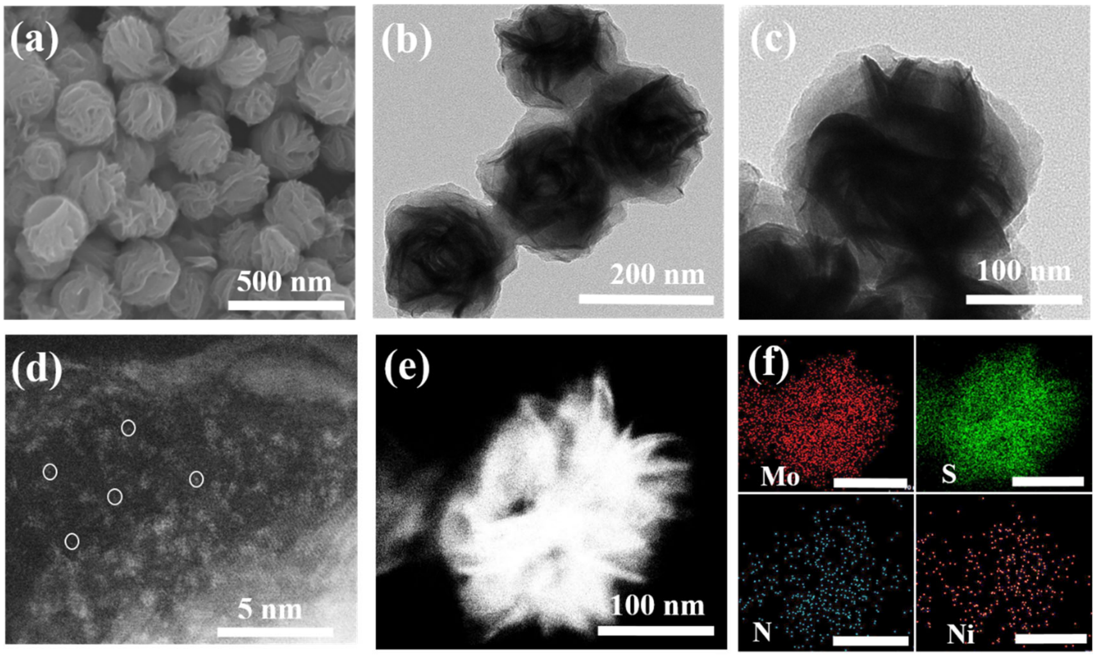

Figure S6. (a) SEM image and TEM images of MoS$_2$@Ni-N-C NSs at (b) low and (c) high magnifications, respectively. (d) Aberration-corrected (AC) HAADF-STEM image of MoS$_2$@Ni-N-C NS. (e) High angle annular dark field scanning TEM (HAADF-STEM) image and (f) element maps (Mo: red, S: green, N: blue, Ni: orange; scale bar = 100 nm) of MoS$_2$@Ni-N-C NS.

The HAADF-STEM images of MoS$_2$@Ni-N-C NSs present atomically-dispersed species in the carbon substrate. The element mapping results reveal the homogeneous distribution of Mo, S, N and Ni elements in the respective NSs (**Figure S6f**). These results suggest that single Ni atoms were successfully anchored on the N-doped carbon matrix.

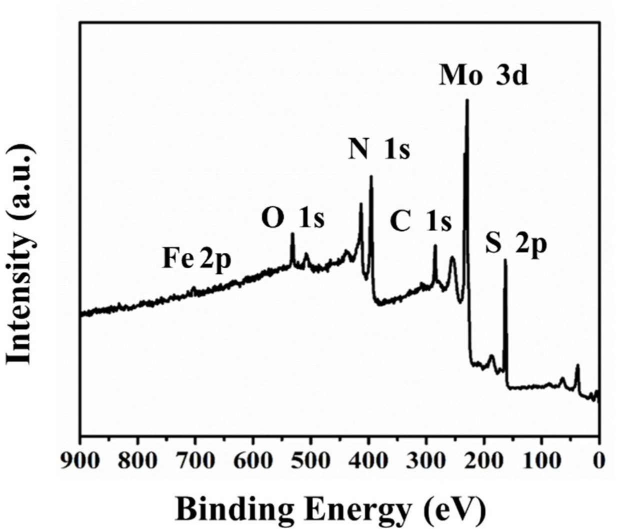

Figure S7. XPS survey spectrum of MoS_2@Fe-N-C NSs.

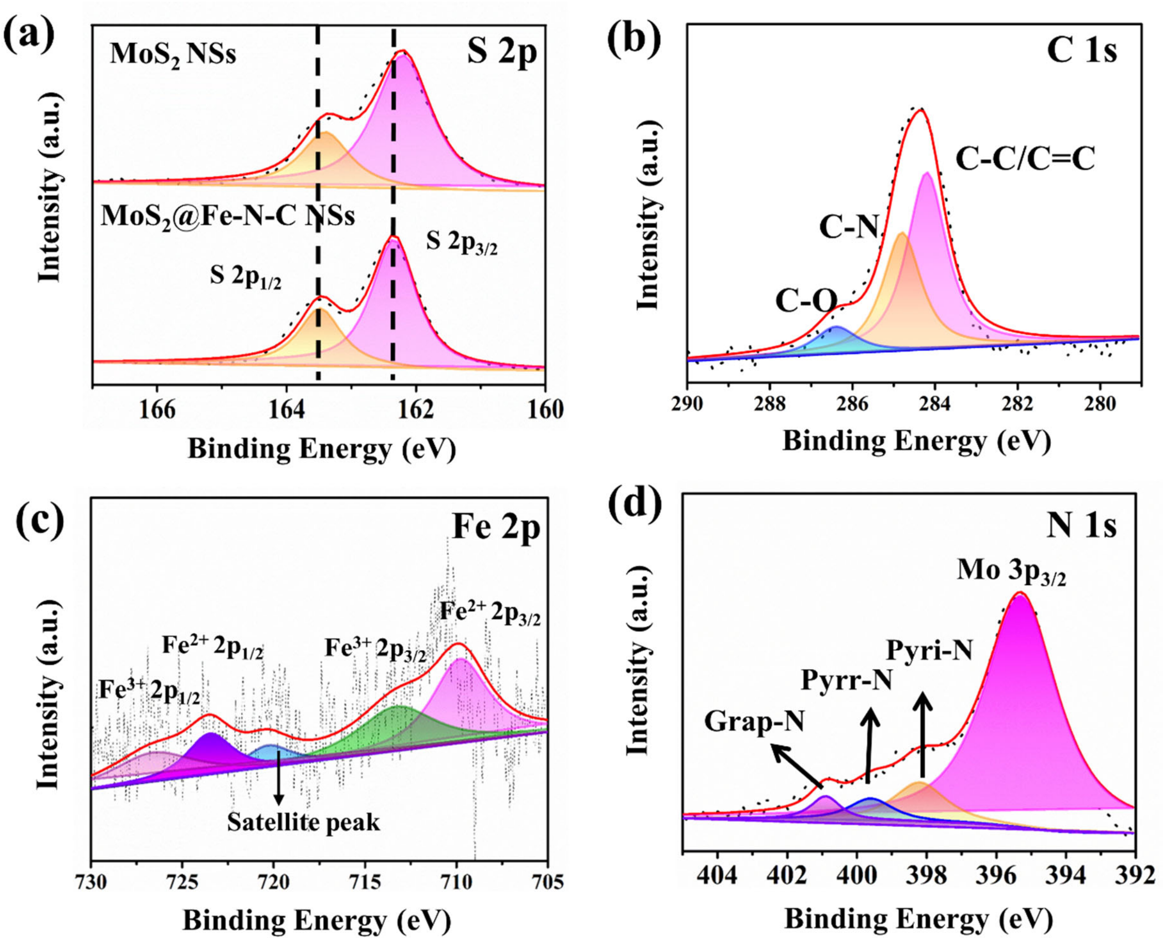

Figure S8. High-resolution (a) S 2p, (b) C 1s, (c) Fe 2p, and (d) N 1s XPS spectra, respectively.

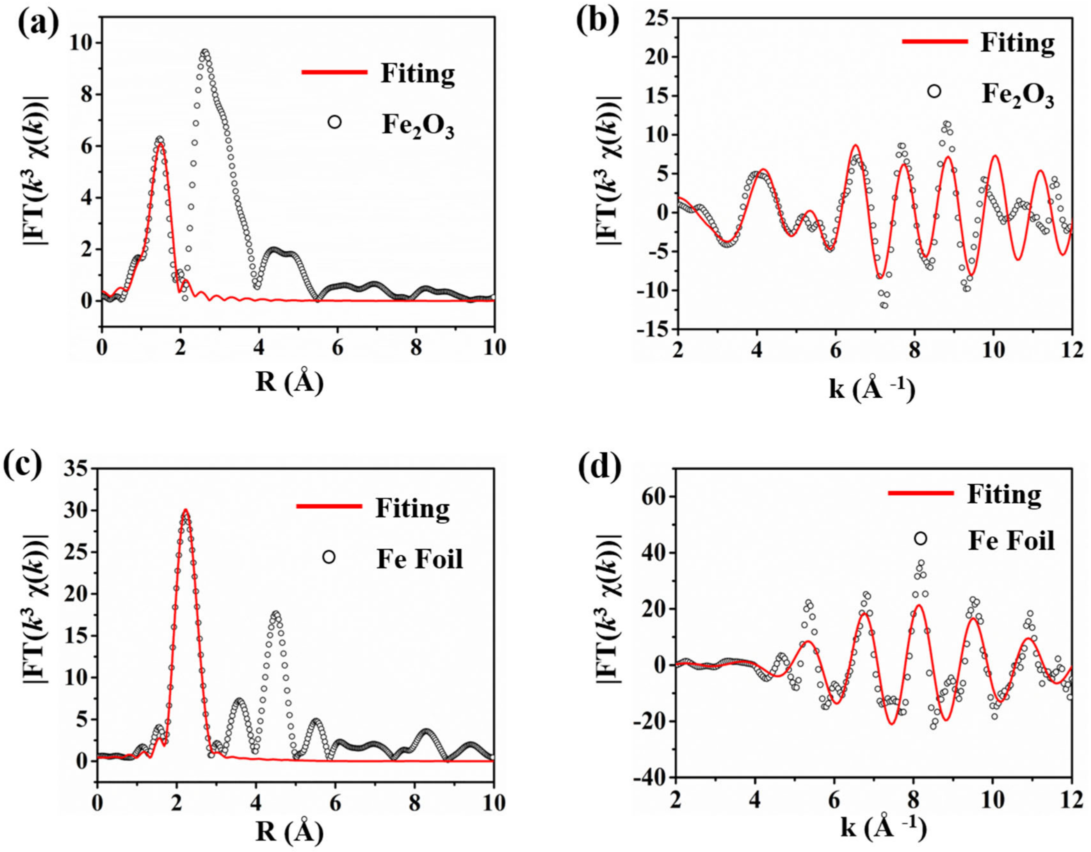

Figure S9 (a) The corresponding extended X-ray absorption fine structure (EXAFS) R space fitting curve of Fe_2O_3. (b) The corresponding EXAFS k space fitting curve of Fe_2O_3. (c) The corresponding EXAFS R space fitting curve of Fe foil. (d) The corresponding EXAFS k space fitting curve of Fe foil.

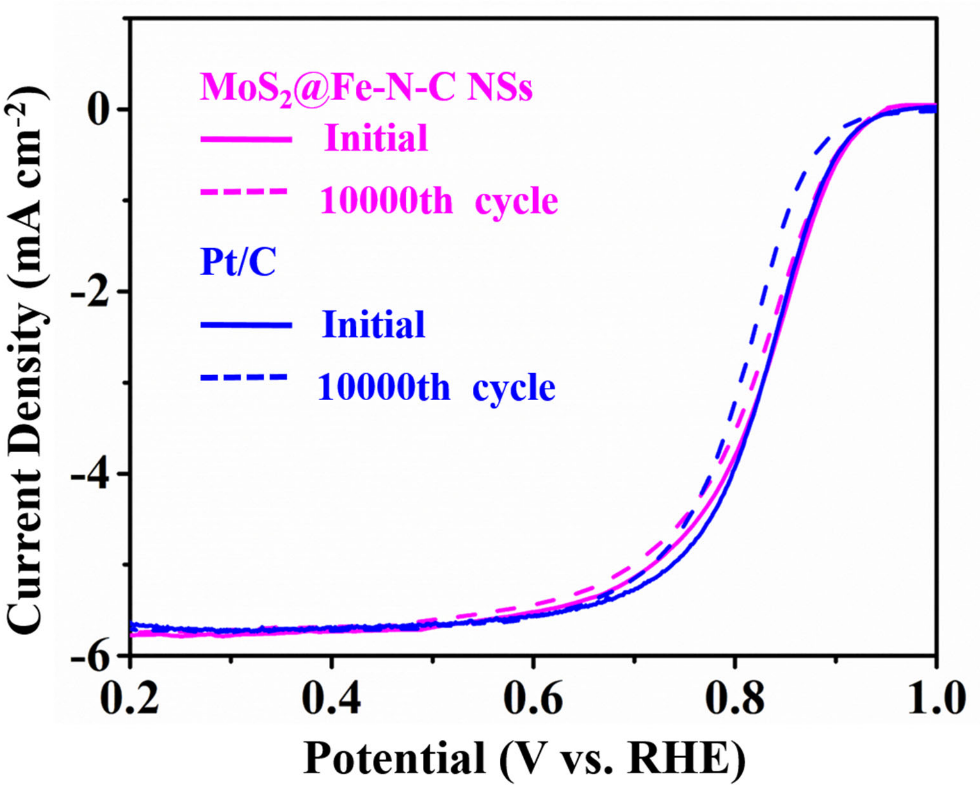

Figure S10. Polarization curves of MoS_2@Fe-N-C NSs and Pt/C before and after 10000 potential sweeps at 50 mV s^{-1} for ORR test.

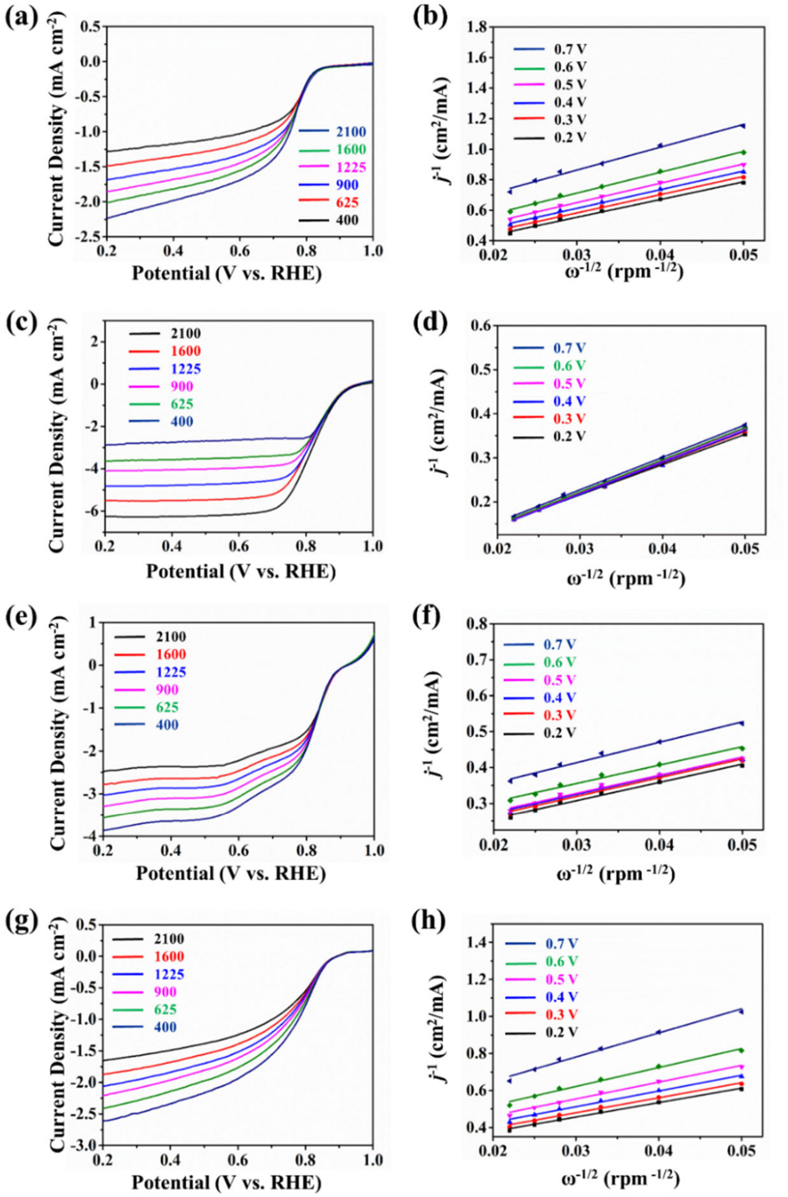

Figure S11. (a) Rotating disk electrode (RDE) polarization curves at different rotating speeds and (b) the corresponding Koutechy-Levich plots for MoS_2 NSs. (c) RDE polarization curves at different rotating speeds and (d) the corresponding Koutechy-Levich plots for MoS_2@Fe-N-C NSs. (e) RDE polarization curves at different rotating speeds and (f) corresponding Koutechy-Levich plots for MoS_2@Co-N-C NSs. (g) RDE polarization curves at different rotating speeds and (h) the corresponding Koutechy-Levich plots for MoS_2@Ni-N-C NSs.

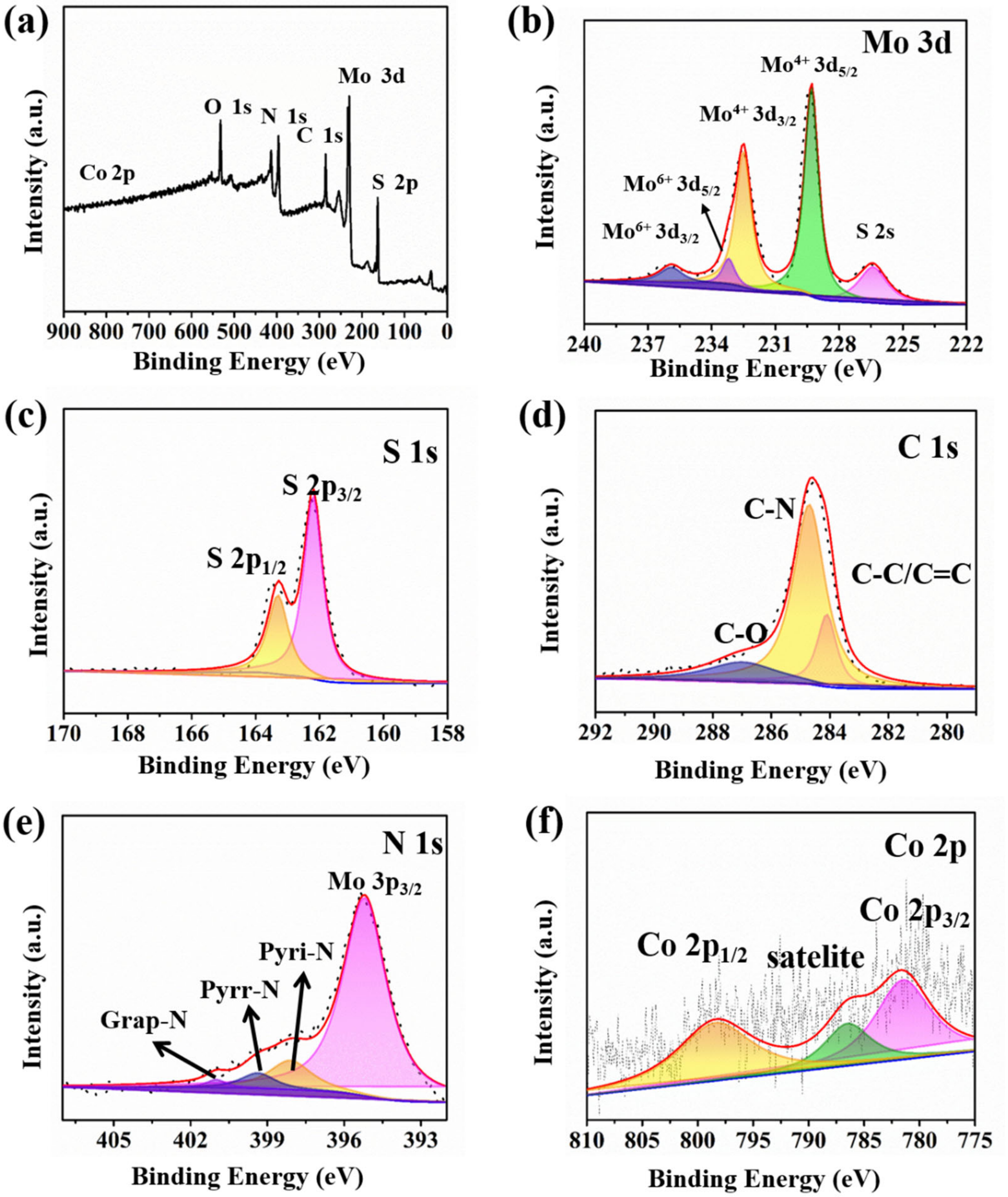

Figure S12. (a) XPS survey spectrum of the MoS$_2$@Co-N-C NSs. High-resolution (b) Mo 3d, (c) S 1s, (d) C 1s, (e) N 1s and (f) Co 2p XPS spectra, respectively.

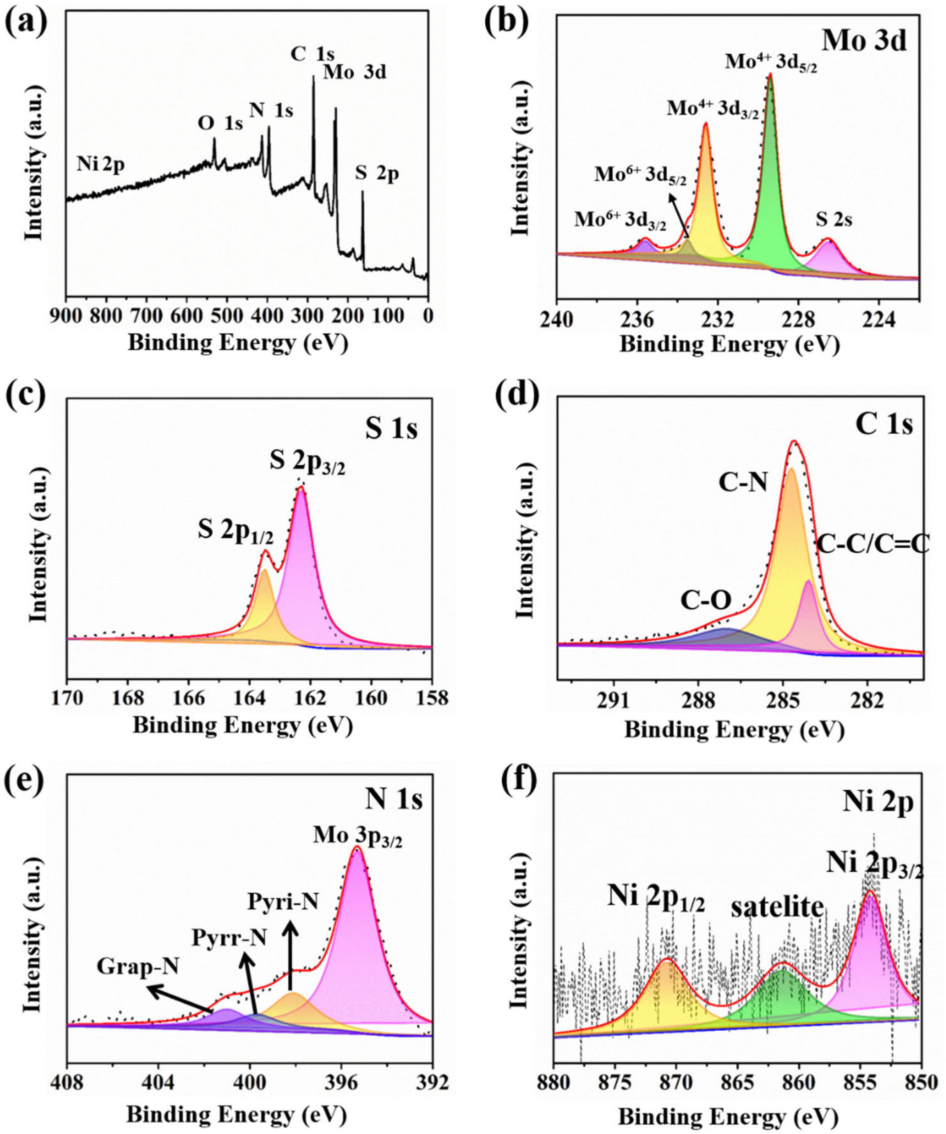

Figure S13. (a) XPS survey spectrum of the MoS_2@Ni-N-C NSs. High-resolution (b) Mo 3d, (c) S 1s, (d) C 1s, (e) N 1s and (f) Ni 2p XPS spectra, respectively.

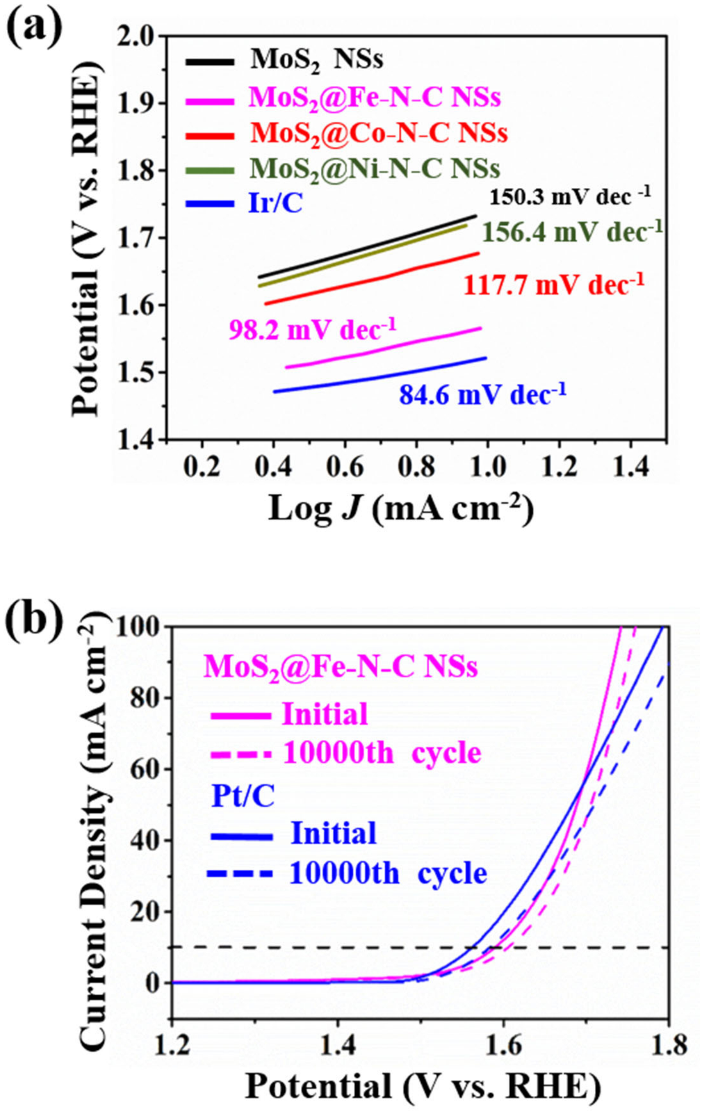

Figure S14. (a) The corresponding OER Tafel slops of MoS_2 NSs, MoS_2@Fe-N-C NSs, MoS_2@Co-N-C NSs, MoS_2@Ni-N-C NSs, and Ir/C, respectively. (b) Polarization curves of MoS_2@Fe-N-C NSs and Ir/C before and after 10000 potential sweeps at 50 mV s^{-1} for OER test.

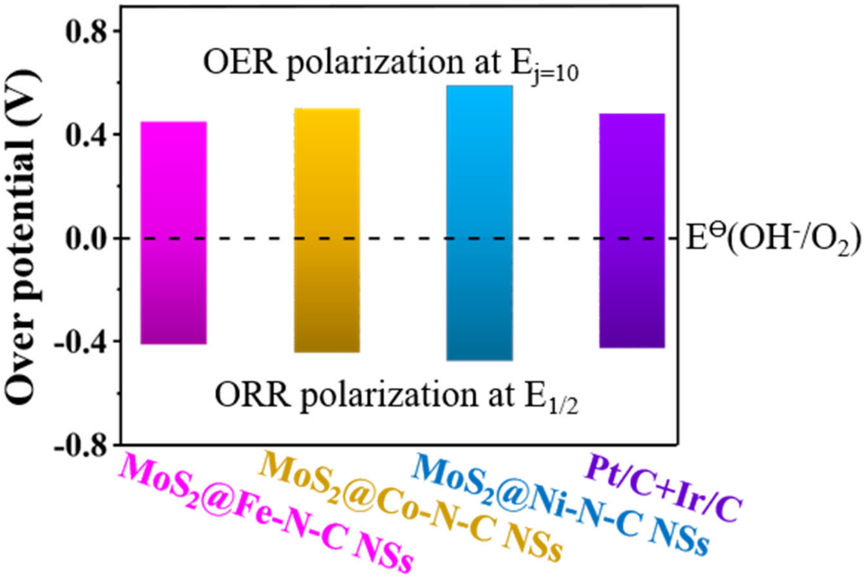

Figure S15. Comparison of oxygen bifunctional catalytic performances of MoS_2@Fe-N-C NSs, MoS_2@Co-N-C NSs, MoS_2@Ni-N-C NSs, and Pt/C+Ir/C

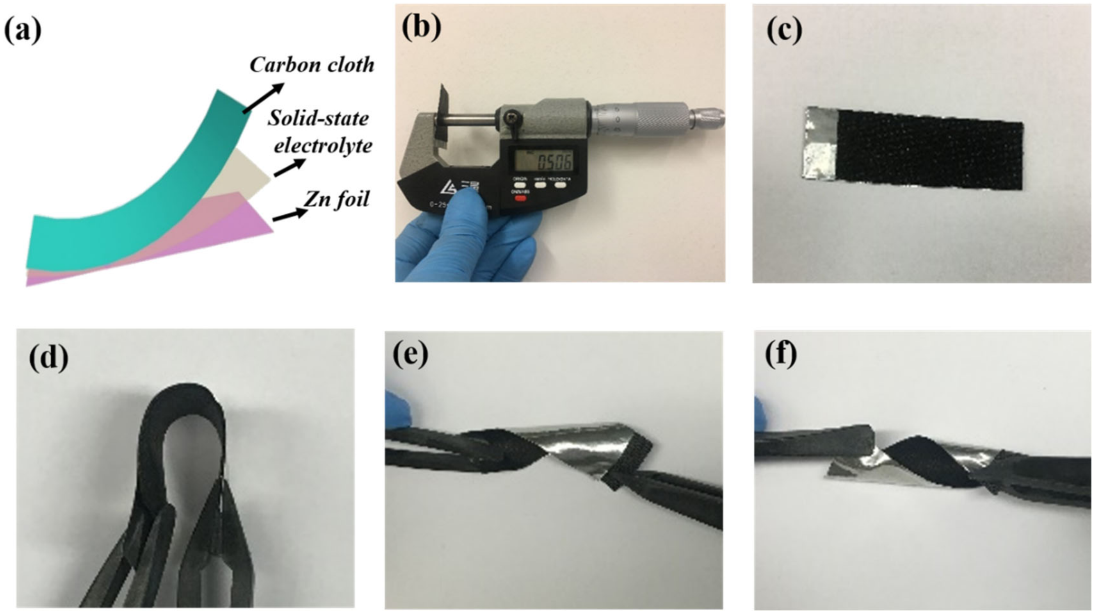

Figure S16. (a) Schematic diagram of a flexible all-solid-state zinc-air battery (ZAB). (b) Digital image showing the thickness of the all-solid-state ZAB (0.506 cm), measured by micrometer caliper. Digital images of (c) flat ZAB, (d) bended ZAB (180°), (e) twisted ZAB, and (f) heavily twisted ZAB, respectively.

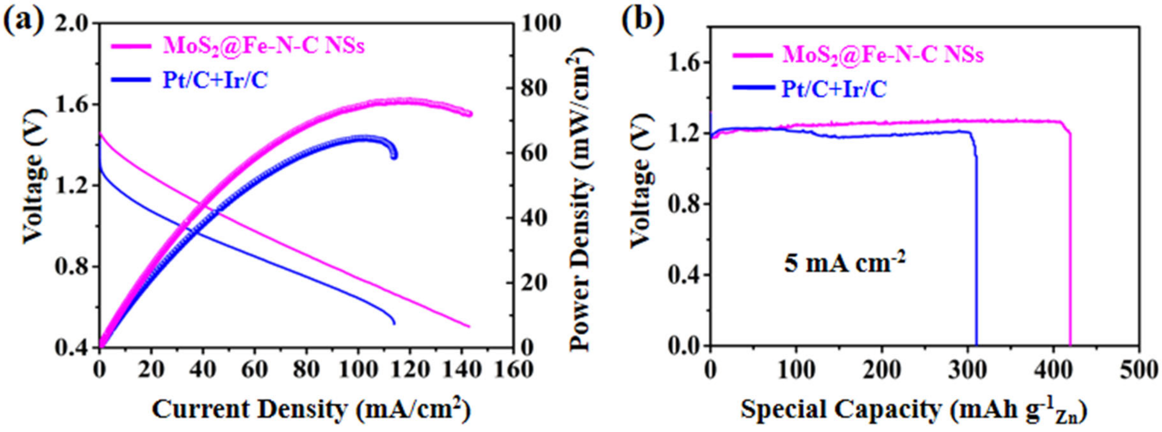

Figure S17. (a) Discharging polarization curves and the corresponding power densities. (b) The voltage–capacity curves of Zn–air batteries based on the MoS_2@Fe-N-C NSs and Pt/C+Ir/C cathode catalysts at the current density of 5 mA cm^{-2}.

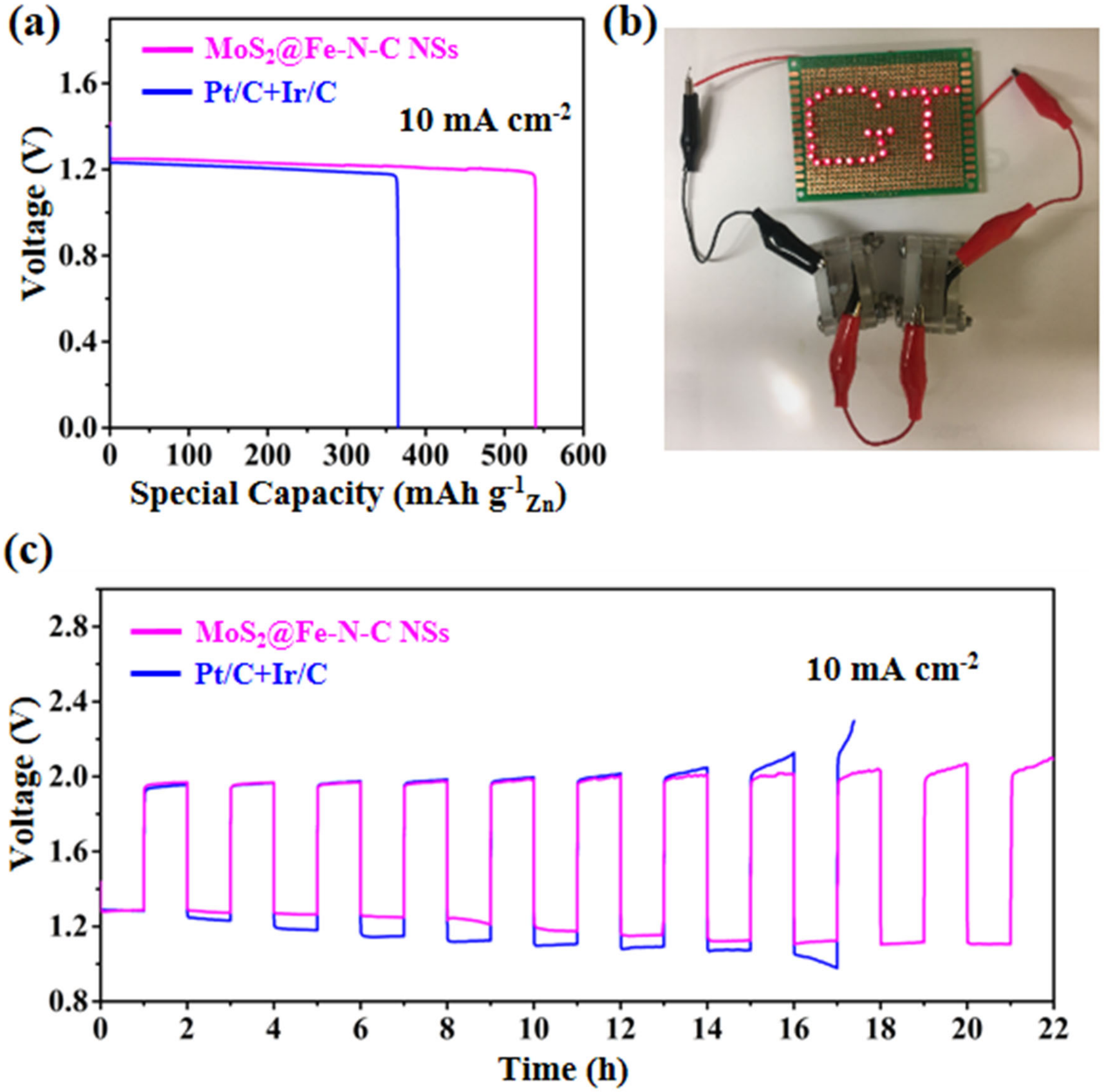

Figure S18. (a) The voltage–capacity curves of Zn–air batteries (ZABs) based on MoS_2@Fe-N-C NSs and Pt/C+Ir/C cathode catalysts at the current density of 10 mA cm^{-2}. (b) Digital image of two ZABs in series that light an array of red LEDs. (c) The stability curves of ZABs based on MoS_2@Fe-N-C NSs and Pt/C+Ir/C cathode catalysts at the current density of 10 mA cm^{-2}.

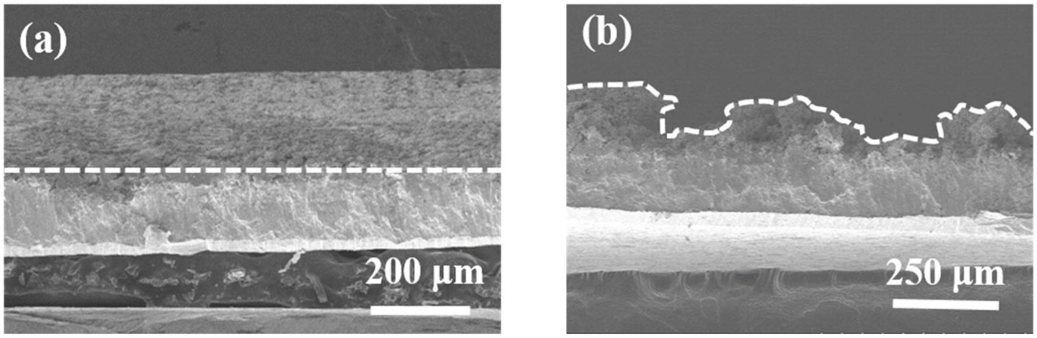

Figure S19. SEM images of zinc foil after the cycling stability test of (a) MoS_2@Fe-N-C NSs-based ZAB and (b) Pt/C+Ir/C-based ZAB after 18 h cycling.

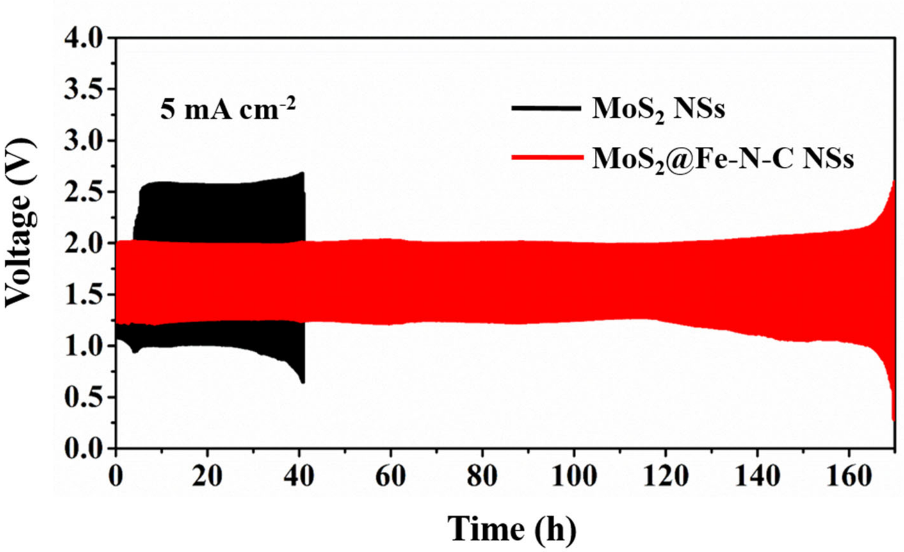

Figure S20. The stability curves of the MoS$_2$-based ZAB and MoS$_2$@Fe-N-C-based ZAB at a constant current density of 5 mA cm^{-2}.

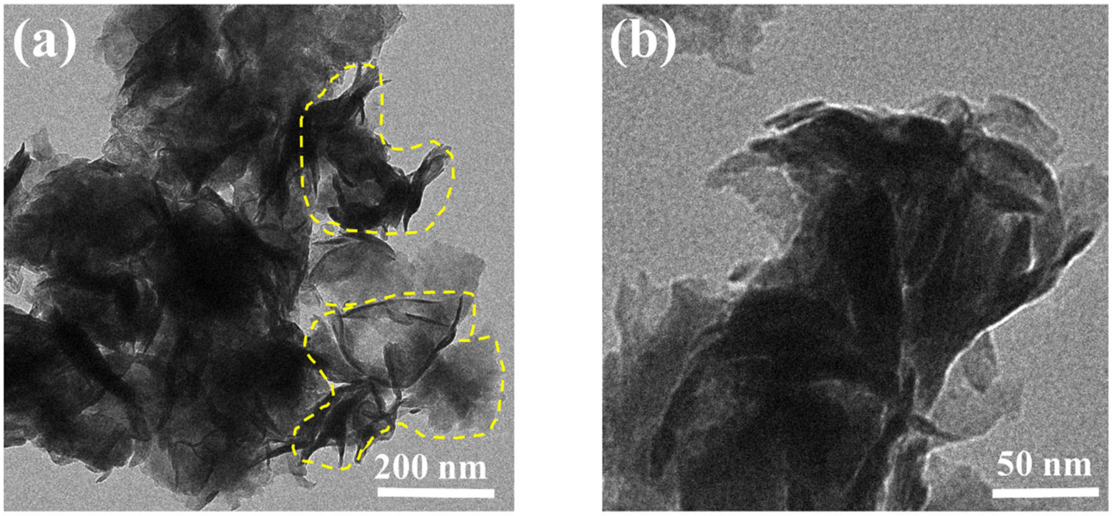

Figure S21. TEM image of MoS_2 cathode after being cycled for 120 times, where the collapsed nanospheres are marked with yellow dashed circles.

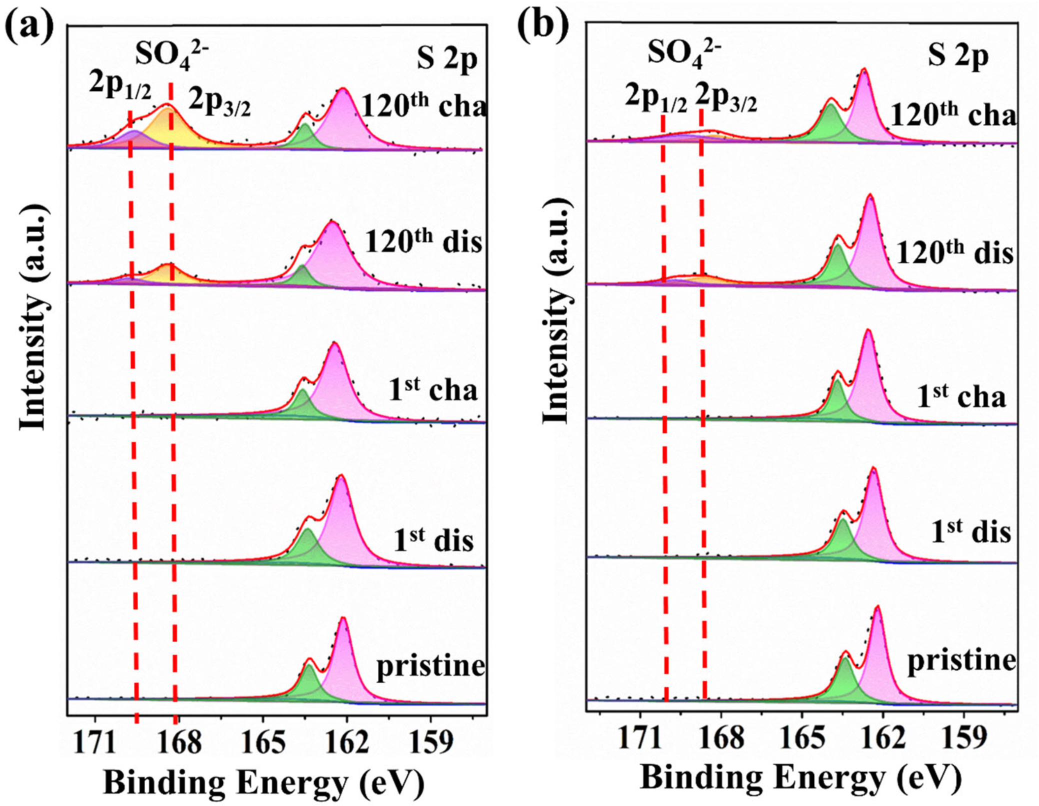

Figure S22. High-resolution S 2p XPS spectra of (a) MoS_2 cathode and (b) MoS_2@Fe-N-C cathode obtained from the 1st discharge, 1st charge, 120th discharge, and 120th discharge processes.

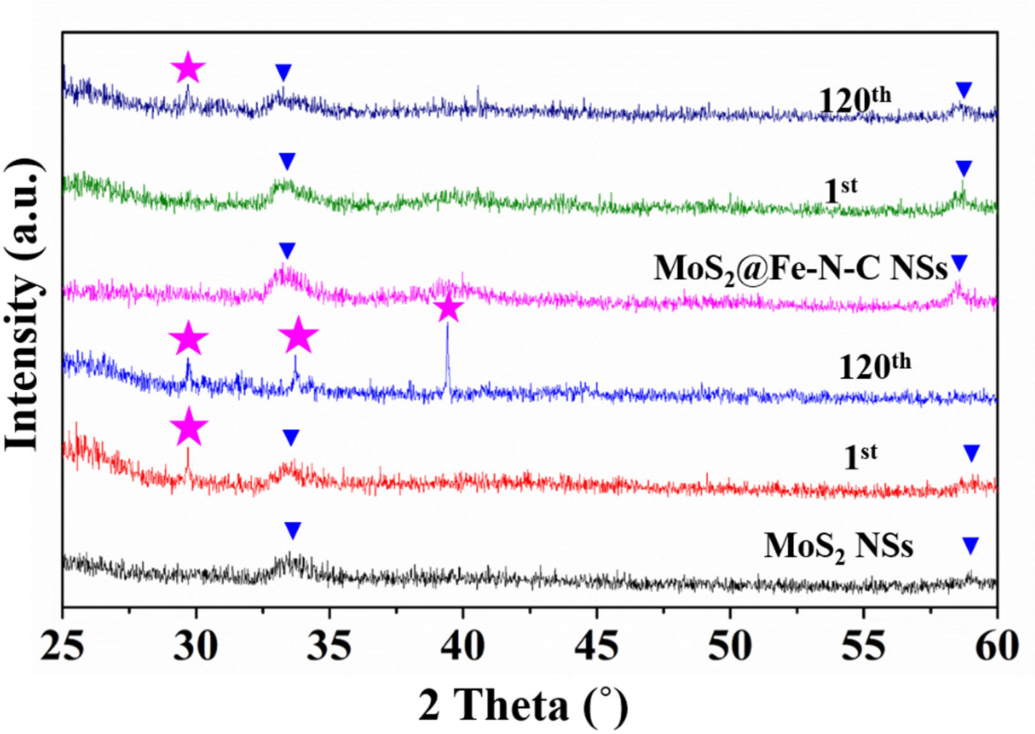

Figure S23. XRD patterns of the MoS$_2$-based electrodes and the MoS$_2$@Fe-N-C-based electrodes obtained from the1st and 120th cycles (Stars: characteristic diffraction peaks of MoO$_3$. Triangle: characteristic diffraction peaks of MoO$_3$ of MoS$_2$).

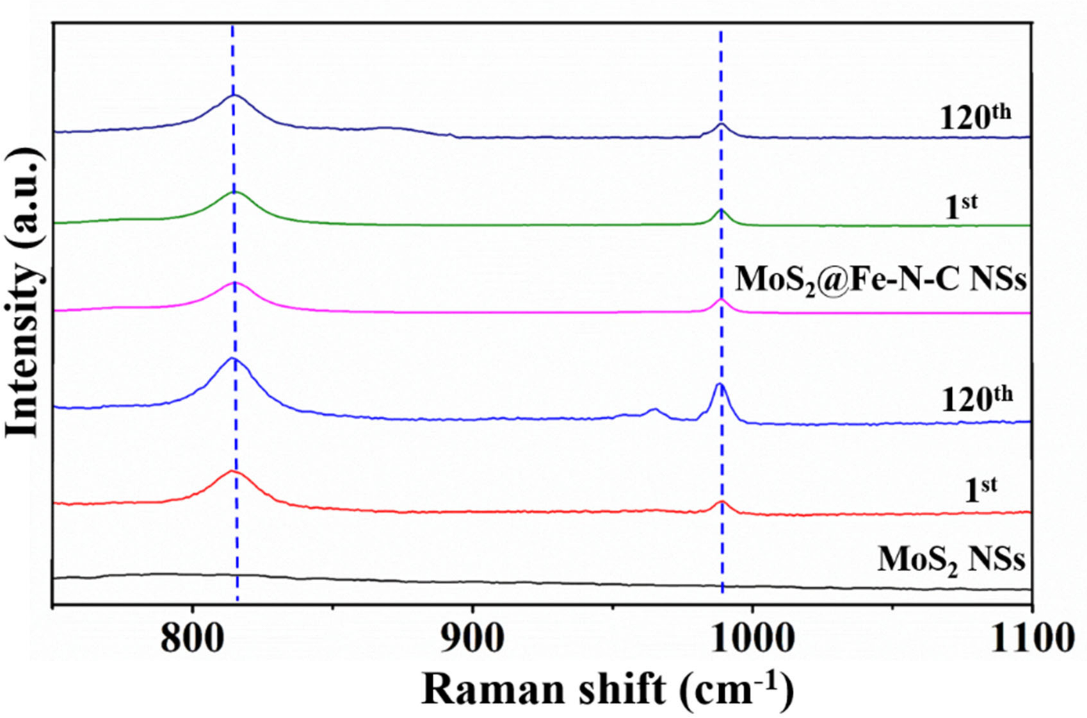

Figure S24. Raman spectra of the MoS_2-based electrodes and the MoS_2@Fe-N-C-based electrodes obtained from the 1st and 120th cycles.

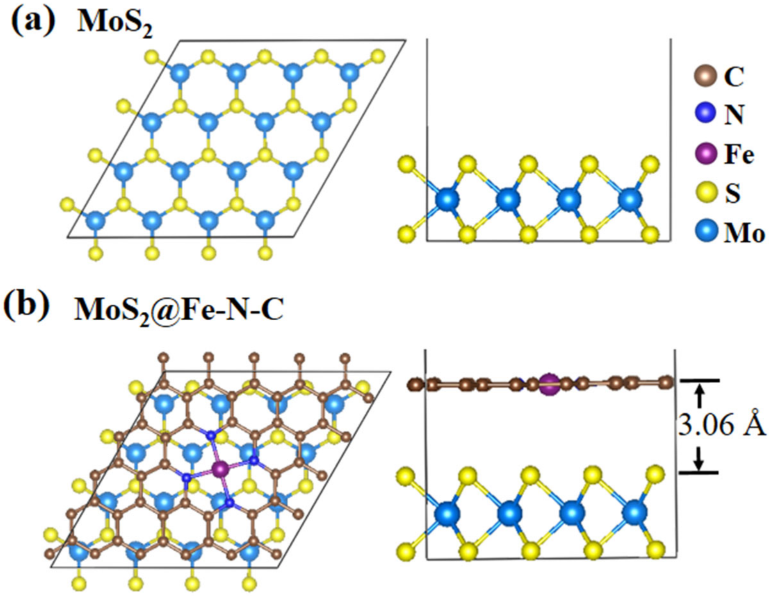

Figure S25. Top view and side view of structural models of (a) MoS$_2$ and (b) MoS$_2$@Fe-N-C, respectively.

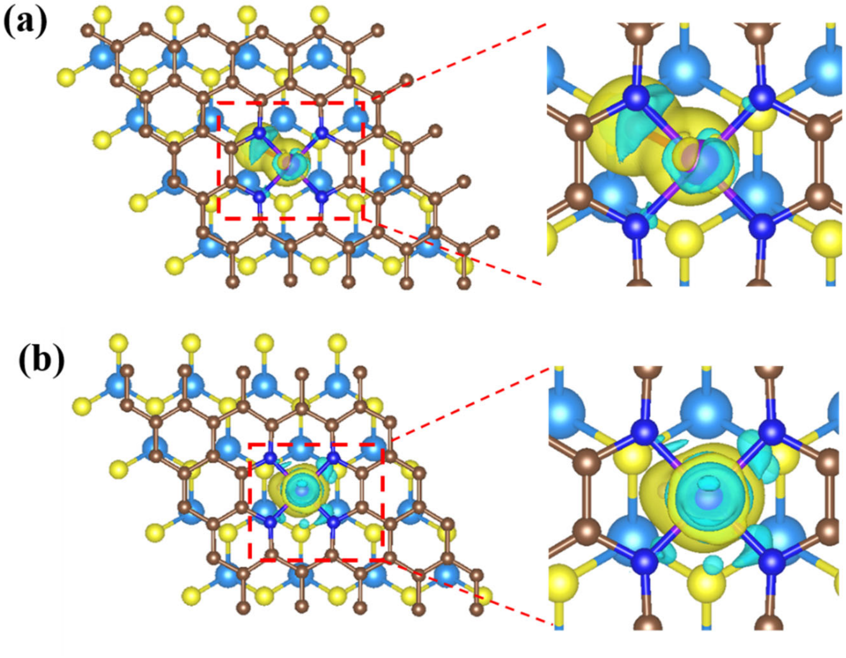

Figure S26. Top view of electron density difference plots for MoS_2@Fe-N-C with adsorbed (a) O_2 and (b) OH, respectively. The isosurface value of yellow and cyan regions are 0.003 $Bohr^{-3}$. Yellow contours represent the charge accumulations, and cyan contours denote the charge depletion.

Table S1. Structural parameters of MoS_2@Fe-N-C NSs, Fe foil, and Fe_2O_3 extracted from the EXAFS fitting. (S_0^2=0.72)

Samples	Shell	N^a	$R(Å)^b$	$\sigma^2\times10^3(Å^2)^c$	ΔE_0 (eV)^d	R factor
Fe foil	Fe-Fe1	8	2.47	4.9	4.5	0.004
	Fe-Fe2	6	2.84	6.2		
Fe_2O_3	Fe-O1	3	1.99	5.4	2.6	0.015
	Fe-O2	3	1.92	4.5		
MoS_2@Fe-N-C NSs	Fe-N	4	2.02	4.3	2.7	0.004

$^a N$: coordination number; $^b R$: bond distance (the bond length between the central atoms and surrounding coordination atoms); $^c\sigma^2$: Debye-Waller factors (a measure of thermal and static disorder in absorber-scatterer distance); ^{d} ΔE_0: the inner potential correction. *R* factor: goodness of fitting.

Table S2. Gibbs free energies of four elementary steps in ORR processes for MoS_2, MoS_2@Fe-N-C surface (denoted MoS_2@Fe-N-C Sur), and MoS_2@]Fe-N-C interface (denoted MoS_2@Fe-N-C Int), respectively.

	ΔG_1 *(eV)*	ΔG_2 *(eV)*	ΔG_3 *(eV)*	ΔG_4 *(eV)*
MoS_2	-0.173	-2.650	0.760	1.337
MoS_2@Fe-N-C Sur	-0.847	-2.119	-0.957	-0.997
MoS_2@Fe-N-C Int	-0.905	-1.857	-1.126	-1.032

Table S3. Comparison of performance of all-solid-state ZABs.

Catalysts	Loading density (mg cm^{-2})	Open circuit potential (V)	Power density (mW cm^{-2})	Cycling density (mA cm^{-2})	Cycling stability	Refs
MoS_2@Fe-N-C NSs	**0.25**	**1.47**	**78**	**5**	**20 min/cycle for 50 cycles without visible voltage loss**	**This work**
Mo–N/C@MoS_2	1	1.34	-	2	-	(6)
NC-Co SA	Free-standing	1.41	31.0	1	20 min/cycle for 30 cycles without visible voltage loss	(7)
Co_3O_4@N-CNMAs/CC	1.82	1.461	65	1	20 min/cycle for 24 cycles without visible voltage loss	(8)
CC-AC	Free-standing	1.37	52.3	1	20 min/cycle for 50 cycles without visible voltage loss	(9)
N-GCNT/FeCo	2	1.25	97.8	100	10 min/cycle for 72 cycles without visible voltage loss	(10)
Fe-N_x-C	-	1.49	-	1	Cycling about 120 h without visible voltage loss	(11)
FeN_x-PNC	-	1.43	110	5	11 min/cycle for 220 cycles without visible voltage loss	(12)

Supplementary movies

This supplementary material includes 1 movie file. The detail of this movie is as follows：

Movie S1. Bending test of two flexible ZABs in series with LED lights on.

References

1. Kresse G & Hafner J (1993) Ab initio molecular dynamics for open-shell transition metals. *Phys. Rev. B* 48(17):13115-13118.
2. Perdew JP, Burke K, & Ernzerhof M (1996) Generalized Gradient Approximation Made Simple. *Phys. Rev. Lett.* 77(18):3865-3868.
3. Blöchl PE (1994) Projector augmented-wave method. *Phys. Rev. B* 50(24):17953-17979.
4. Nørskov JK*, et al.* (2004) Origin of the Overpotential for Oxygen Reduction at a Fuel-Cell Cathode. *J. Phys. Chem. B* 108(46):17886-17892.
5. Man IC*, et al.* (2011) Universality in Oxygen Evolution Electrocatalysis on Oxide Surfaces. *ChemCatChem* 3(7):1159-1165.
6. Amiinu IS*, et al.* (2017) Multifunctional Mo-N/C@MoS_2 Electrocatalysts for HER, OER, ORR, and Zn-Air Batteries. *Adv. Funct. Mater.* 27(44):1702300.
7. Zang W*, et al.* (2018) Single Co Atoms Anchored in Porous N-Doped Carbon for Efficient Zinc−Air Battery Cathodes. *ACS Catal.* 8(10):8961-8969.
8. Zhong Y*, et al.* (2019) Hierarchical Co_3O_4 Nano-Micro Arrays Featuring Superior Activity as Cathode in a Flexible and Rechargeable Zinc-Air Battery. *Adv. Sci.* 6(11):1802243.

9. Kordek K*,* *et al.* (2019) Two-Step Activated Carbon Cloth with Oxygen-Rich Functional Groups as a High-Performance Additive-Free Air Electrode for Flexible Zinc-Air Batteries. *Adv. Energy Mater.* 9(4):1802936.

10. Su C-Y*, et al.* (2017) Atomic Modulation of FeCo-Nitrogen-Carbon Bifunctional Oxygen Electrodes for Rechargeable and Flexible All-Solid-State Zinc-Air Battery. *Adv. Energy Mater.* 7(13):1602420.

11. Han J*, et al.* (2019) Single-Atom Fe-N_x-C as an Efficient Electrocatalyst for Zinc–Air Batteries. *Adv. Funct. Mater.* 29(41):1808872.

12. Ma L*, et al.* (2018) Single-Site Active Iron-Based Bifunctional Oxygen Catalyst for a Compressible and Rechargeable Zinc-Air Battery. *ACS Nano* 12(2):1949-1958.